International Journal of Machine Tools & Manufacture 183 (2022) 103957

Contents lists available at ScienceDirect

International Journal of Machine Tools and Manufacture

journal homepage: www.elsevier.com/locate/ijmactool

Keyhole pores reduction in laser powder bed fusion additive manufacturing of nickel alloy 625

H. Yeung *, F.H. Kim, M.A. Donmez, J. Neira

National Institute of Standards and Technology, Gaithersburg, MD, 20899, USA

ARTICLE INFO

Keywords:
Keyhole pores
Scan strategies
X-ray computed tomography
Digital twins

ABSTRACT

Keyhole pores are common in additively manufactured parts and can badly deteriorate the part's performance. In this study, we demonstrated that the keyhole pores formation in the laser powder bed fusion additive manufacturing process can be significantly reduced by the constant laser power density scan strategy. The constant laser power density is implemented on a custom-built testbed by continuously varying the laser power with the laser scan speed through the time-stepped digital commands developed. Two cubic nickel alloy 625 parts of identical geometry were built, one with the constant laser power density scan strategy, and another with the conventional constant laser power scan strategy. The X-ray computed tomography (XCT) measurement shows a 67% porosity reduction in the part built with constant laser power density. However, the mechanisms for defect formation are not easily distinguishable in XCT, which gives a 'total' count of pores. To further investigate the effect of scan strategies on pore formation, two digital twins of process monitoring (DTPM), meltpool intensity volume (MPIV) and melt pool area volume (MAV), were created. The DTPM not only helps to distinguish the keyhole pores from the lack of fusion defects but also provides a foundation for the future development of machine learning models.

1. Introduction

Laser powder bed fusion (LPBF) is an additive manufacturing (AM) process in which a focused laser beam selectively melts geometric patterns in layers of metal powders and builds parts layer by layer. The part quality is determined by many process parameters [1–5] such as the laser scan path, power, speed, hatch spacing, and gas flow. Porosity is one of the important part quality metrics, and pore formation has been attributed to various phenomena related to the power-speed (P–V) settings, such as insufficient melting of the metal powder (i.e., lack of fusion pores) [6,7], or keyhole collapse at high laser energy densities (i.e., keyhole pores) [8,9]. Khairallah et al. noted that abruptly turning the laser off at the end of a scan vector can potentially cause pores to be trapped under the rapidly solidified melt pool, and they recommended laser power reduction at these locations [10]. Shrestha et al. characterized the keyhole pore formation with single-track scanning and micro-CT analysis and found a significant increase in pore volume at lower scanning speeds [11].

Direct observations of keyhole pore formation in the LPBF AM process were made in more recent studies by using in-situ high-energy X-ray radiography. Martin et al. found that reversing the laser scan direction at the end of a scan causes pores to be formed within 300 μm under the solidified melt pool [12]. It is attributed to the overheating caused by the increase of instantaneous laser power density when the scan speed approaches zero at the turning point. Cunningham et al. plotted the keyhole morphologies across P–V space [13] and showed deep keyholes could occur at laser power as low as 150 W if the speed was also low (less than 500 mm/s). Hojjatzadeh et al. made an excellent summary of different pore formation mechanisms and frequently observed the formation of keyhole pores at the end of the track when the laser was switched off [14]. Guo et al. revealed that keyhole oscillation is one of the three major mechanisms for causing melt flow instabilities in the LPBF process [15]. Wang et al. simulated the keyhole pore formation with a multiphysics thermal-fluid flow model [16]. The results were validated with the in-situ X-ray images of single-track scans and suggest the keyhole pore is very sensitive to the laser power and speed parameters. However, in-situ high-speed X-ray imaging of 3D builds is very challenging and no such study is found in literature.

In a laser powder bed fusion process, the laser power density is proportional to the ratio of laser power to the laser scan speed [17].

* Corresponding author.
E-mail address: ho.yeung@nist.gov (H. Yeung).

https://doi.org/10.1016/j.ijmachtools.2022.103957
Received 25 May 2022; Received in revised form 3 October 2022; Accepted 15 October 2022
Available online 22 October 2022
0890-6955/Published by Elsevier Ltd.

Overall, the in-situ x-ray imagining studies show that a keyhole mode can be triggered if the laser power density is high. While the laser power can be kept relatively constant, the laser scan speed is varying (from 0 to the steady state speed) during the transient state while it is still accelerating/decelerating. If the laser power is constant for the whole scan, the laser power density will become excessively high during the transient state and likely to create keyhole pores at the end of the scan tracks [12]. In three-dimensional (3D) builds, especially for parts built with island scan strategies, the tracks could end inside the part geometric boundaries (at the junction of the island boundaries) and the keyhole pores formed would be buried inside the parts that cannot be removed by post surface processing such as machining or polishing. Unlike lack of fusion (LOF) pores, keyhole pores are also unlikely to be healed by re-melting from the layers above because they are too deep. Therefore, it is important to prevent keyhole pore formation in the first place.

Martin et al. [12] demonstrated that the keyhole mode can be prevented at end of a scan by keeping laser power density relatively constant. However, very few applications of this method to 3D builds can be found. There could be two major challenges. First, the constant power density scan strategy requires the laser power to be continuously proportional to the scan speed. Most of the state of arts commercial LPBF AMmachines do not even support a continuous laser power variation within a scan vector. Custom-built testbeds may provide such control, but often lack software supporting the 3D scan path planning/interpolation. Second, the constant laser power density scan strategy lowers the laser power when the scan speed is low. This may trigger LOF pores, especially if the laser power-speed synchronization is not precise, the actual P–V parameters can easily fall into the LOF processing window [17]. X-ray computed tomography (XCT) is often used for porosity measurement, but XCT alone may not be able to distinguish whether a pore is LOF or a keyhole. New methods will be required to identify keyhole pores efficiently in 3D parts.

A digital twin is defined as a digital representation of assets, processes, or systems [18]. Various studies were undertaken to develop this technology for AM. DebRoy and his co-workers carried out pioneering work in the construction of digital twins for AM process [19–21]. They suggest that a digital twin of 3D printing hardware consists of a mechanistic model, a sensing and control model, a statistical model, big data, and machine learning. They also present a framework of mechanistic models to predict the meltpool-level phenomena and estimate the metallurgical attributes such as the transient temperature field, solidification morphology, grain structure, phases present, and susceptibilities to defect formation. The inputs to these mechanistic models include printing technique, process parameters, and material properties. It is a very comprehensive framework, but it may not be able to predict the defects caused by the stochastic nature of the AM process such as keyholes and spatter [22,23]. In this study, we propose a digital twin of process monitoring (DTPM) and demonstrate its potential application for such defect predictions.

This study focuses on the reduction of keyhole pores in 3D builds, rather than the mechanism of keyhole formation. As mentioned earlier, mechanism of keyhole formation is usually studied through high-fidelity simulations and/or in-situ high-speed x-ray imaging [10–16] of a single-track scan. In this study, 3D parts were successfully built with the constant laser power density scan strategy. The porosity was measured by XCT and compared with parts built with the conventional scan strategy. Digital twins of process monitoring (DTPM) were also created, to predict whether the pores measured by XCT are due to LOF or keyholing. The rest of this paper is organized as follows. The detail on scan strategy implementation and in-situ meltpool monitoring is explained in Section 2. The part dimension and scan path design information are provided in Section 3. Next, in Section 4 and Section 5 the XCT and DTPM are used to study the parts, respectively. The detail of the DTPM construction is also given in Section 5. Finally, conclusions and future work are made in Section 6.

2. AM process control and monitoring

On a typical LPBF AM system, the laser beam is directed to the build platform by a pair of mirrors driven by galvanometer (galvo) motors as shown in Fig. 1a. By moving each mirror in a coordinated manner, the system creates a programmable laser scan path on each layer of powder on the build platform. When the laser beam moves across the powder layer, it melts the metal powder in selected regions, which then cools and solidifies. Each solidified layer may constitute multiple such selected regions or scan patterns sometimes called stripes, islands, etc. To completely melt and solidify the selected regions, the laser beam must move in multiple directions involving frequent changes in direction. Due to moments of inertia of the galvo mirror and its motor coil, a distance is needed for the laser to decelerate to a full stop from steady-state speed. Fig. 1b shows how this situation is handled by the two different control modes [26]. The exact stop mode decelerates the galvo mirrors before the laser reaches the boundary of the scan pattern and stops the laser at the boundary. The constant build speed mode, on the other hand, decelerates the galvo mirrors after the laser passes the part boundary and stops the laser outside the boundary. In both cases, laser power is switched off when the laser beam reaches the scan boundary. Similarly, a distance is needed for the laser to accelerate to steady-state speed, as shown in Fig. 1b where the pseudo color shows the variation in speed.

The exact stop mode is more tolerant to the synchronization error [7] between the laser power and position since the laser is turned on/off when the speed is very slow. The exact stop mode is also faster in terms of the total build throughput as the total traveling distance is shorter, as shown in Fig. 1b. However, the exact stop mode builds parts with slower speeds near the boundaries. If the laser power is constant, there would be a concentration of energy due to the reduced speed, which could lead to the formation of keyhole pores [12,15]. To overcome this limitation, we introduced the constant power density mode, in which the laser power is adjusted based on changing scan speed when approaching the scan boundaries, as shown in Equation (1).

$$L = (V / V_n) \cdot C \cdot L_o + (1 - C) \cdot L_o \tag{1}$$

where L_o is the nominal laser power in W, L is the applied laser power in W, V is the instantaneous speed in mm/s, V_o is the nominal speed in mm/s, and C is a unitless weighting factor between 0 and 1. C is used to maintain a minimum laser power level by varying only a portion of the power to the speed since power should not drop below a threshold where the powder will not melt at any speed.

Equation (1) is used to implement the constant power density mode on the Simple AM (SAM) software [27] developed to control the custom-built Additive Manufacturing Metrology Testbed (AMMT) [28] at the National Institute of Standards and Technology (NIST). SAM reads stereolithography (STL) files and generates time-stepped digital commands that can be executed directly on the AMMT. The time-stepped digital commands is an n x m numerical array as shown in Fig. 2a, where n is the number of steps and m is the number of control parameters. The command is created based on the xy2-100 protocol [29], which updates X and Y galvo positions at a rate of 100 kHz, or each 10 μs time step. At each time step, it also updates the laser power (L), laser spot diameter (D), and trigger status (T). The trigger status parameter is used to generate a signal to synchronize in-situ monitoring devices (Fig. 2b), such as the MP monitoring (MPM) camera, with instantaneous scan position. The emitted light from the MP, which is filtered at 850 nm (±20 nm bandwidth), is directed by a dichroic mirror to the camera sensor with nominal 1:1 magnification and 8 μm pixel size.

The example digital command array in Fig. 2a shows that at the beginning, the laser power (L) increases from 0 to 150 W as the scan speed increases from 0 mm/s to 1500 mm/s. Since X is all 0, the scan speed here is $(y_{i+1}\text{-}y_i)/10^{-5}$ mm/s, where y_i is the value on ith row of Y. This shows how the constant laser power density scan strategy can be

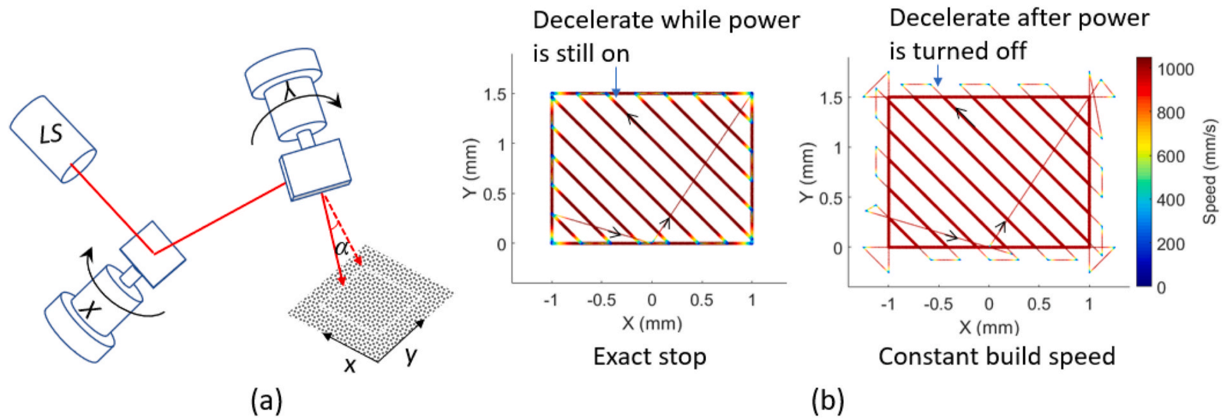

Fig. 1. (a) Illustration of the galvo system. LS is the laser source, galvo (X) controls the laser in the x direction, and galvo (Y) controls the y direction. (b) Scan paths of the exact stop mode and the constant build speed mode. Speed decreases at the beginning and the end of the scan lines due to the acceleration and deceleration. The thicker lines indicate where the laser power is on.

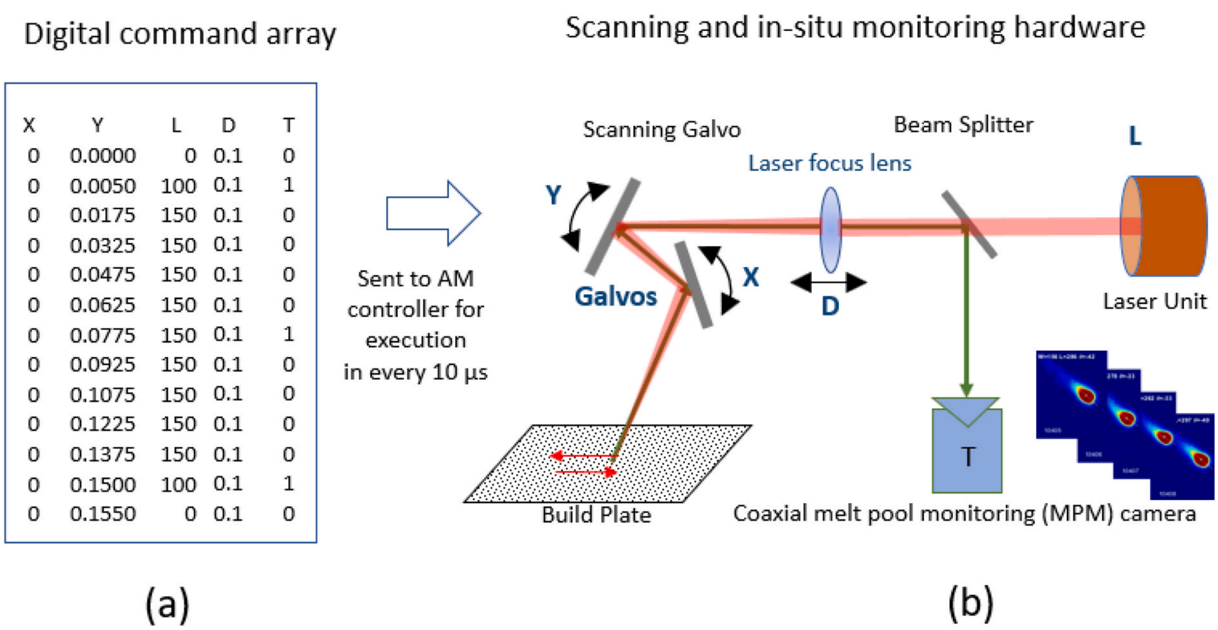

Fig. 2. Time-stepped digital commands and its execution. (a) A sample digital command array. (b) Galvo, laser power, laser diameter, and in-situ monitoring device status are updated every 10 μs? The melt pool monitoring (MPM) camera is triggered by T, which is synchronized with the position.

implemented. In Fig. 2, the camera is triggered every 5 time-steps (hence every 50 μs) as indicated by the 1 in the T column, but it can also be triggered at other frequencies. The laser power feedback, the X and Y galvo encoder feedbacks, and the camera triggers are captured by a high-speed data acquisition (DAQ) system at 100 kHz. A similar array as Fig. 2a is created based on the DAQ data, hence the encoder position at which each image was taken can be mapped. This DAQ array together with the meltpool images consists of the raw data for the DTPM.

3. Experimental procedure

Two IN625 parts of identical geometry were built on AMMT using two different scan strategies: (1) constant power with exact stop mode, and (2) constant power density with exact stop mode. We will simply refer the two scan strategies as constant power scan strategy and constant power density scan strategy in this paper. Fig. 3 shows the part dimensions, and the features at the corners facilitate XCT image alignment to the build orientation. The parts were built with virgin IN625 powder on a 10 cm × 10 cm x 0.64 cm ground substrate of the same material, with a hatch spacing of 100 μm, and a layer thickness of 20 μm. The laser spot size was set to 85 μm. The nominal laser power was 195 W, and the scan speed was 800 mm/s. The build is conducted in an Argon environment with a laminar flow of 280 L/min. The scan region for each part was divided into four islands, with an inter-island rotation of 45°, and inter-layer rotation of 67°. The first two layers of the scan paths are shown in Fig. 4a and b as an example. The size of the islands, the inter-island rotation angle, and the inter-layer rotation angle can be arbitrarily set with the SAM software. The speed profile is identical for both scan strategies. The laser power for the constant power scan strategy is shown in Fig. 4d, and the laser power for the constant power density scan strategy is shown in Fig. 4e. Note the hatching distance plotted in Fig. 4 is 500 μm, instead of 100 μm. This is for better visualization. The pseudo-color in Fig. 4a–c represents speed, and in Fig. 4d–f represents power. The color changes near the boundaries indicate the variation in the laser speed/power. For the constant power density scan strategy, the laser power is lowered when speed slows down, according to Equation (1) with the parameter C = 0.5. The variation of laser power with the scan speed can be visualized in the

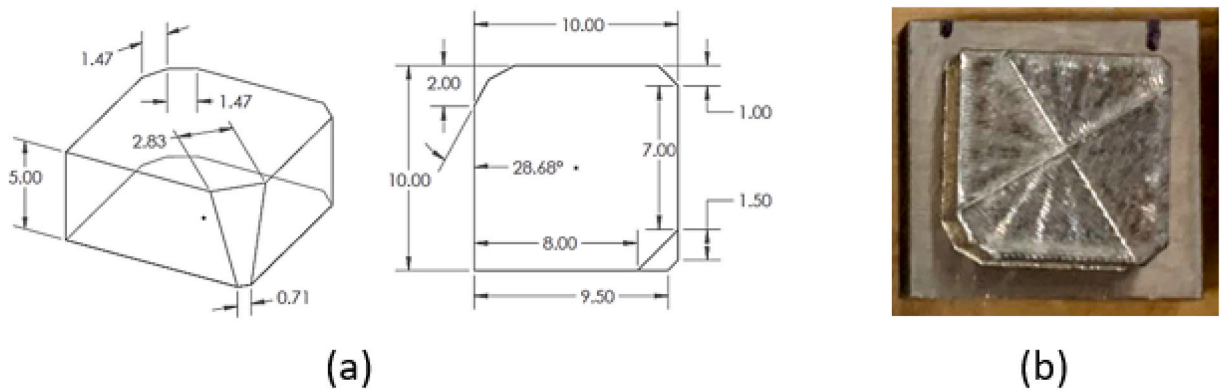

Fig. 3. Part design (a) Illustration of the part dimensions. The features at corners are used for data alignment. The dimensions are in mm. (b) One of the parts built.

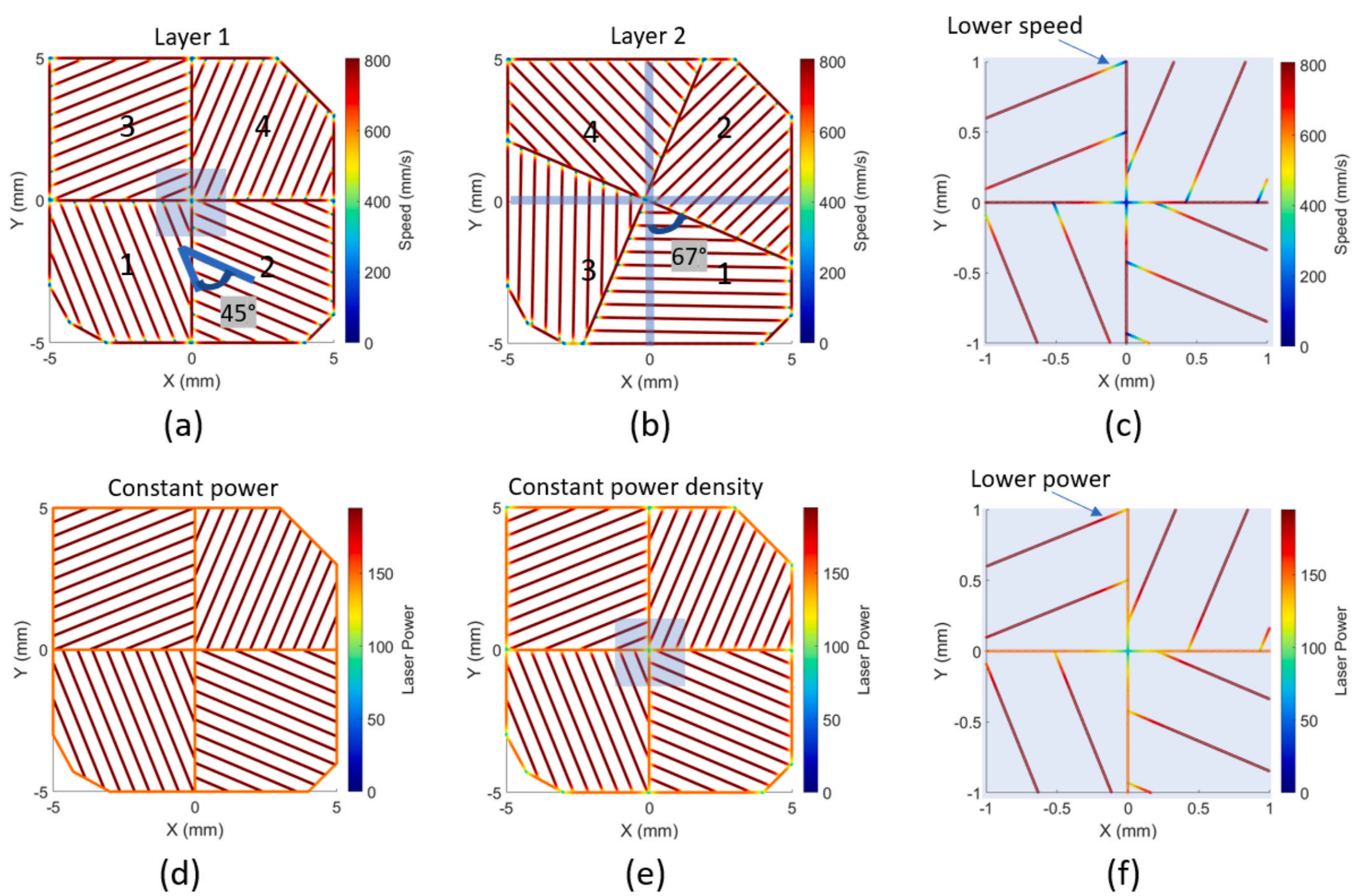

Fig. 4. Scan strategies. (a) Layer 1. (b) Layer 2. (c) Enlarged view of layer 1 near the center. (d) Constant power scan strategy. (e) Constant power density scan strategy. (f) Enlarged view of (e) near the center.

enlarged views in Fig. 4c and f (see Fig. 5).

Since the same scan path and speed were used, the build time for each part is the same. The total laser energy requirement (laser energy input to the build process) can be calculated per Equation (2) below.

$$\text{Energy} = \sum_{i=1}^{n} \left(P_i \cdot 10^{-5}\right) \tag{2}$$

where P_i (J/s) is the power at scan position i, n is the total number of scan points for the part, and $P_i \cdot 10^{-5}$ is the laser energy input during a time step of 10 μs? The laser energy requirement for a part built with the constant power strategy is 85.99 kJ, and for the constant power density strategy is 73.26 kJ, or 15% less. The build process was monitored in-situ by the MP monitoring camera (Fig. 2) with an image capture rate of 10 kHz. XCT scans were also acquired for the parts successfully built from this AM build.

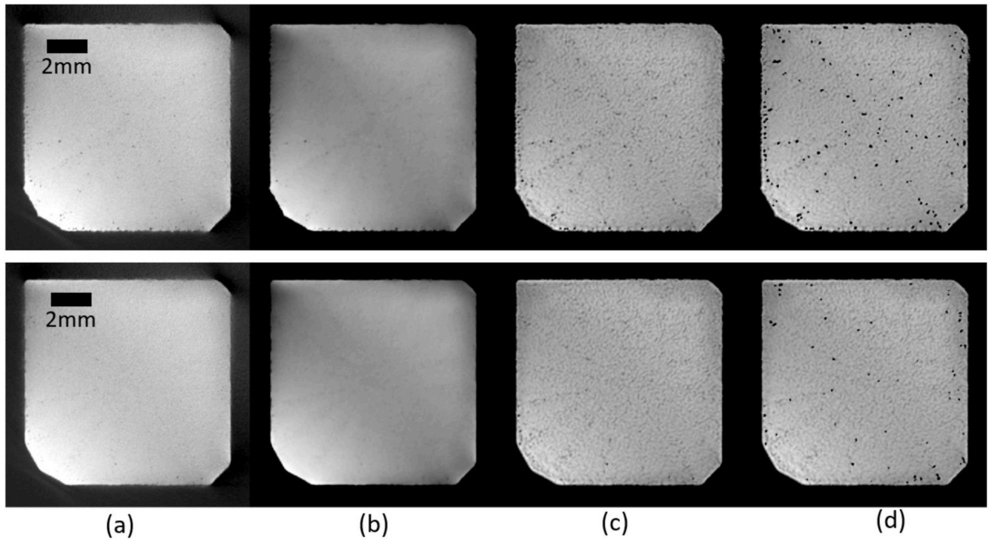

Fig. 5. XCT pores detection. Top row shows the part produced with constant power scan strategy, and bottom row shows the part produced with constant power density scan strategy, both from the same part location. (a) Raw XCT images. (b) Images filtered with an NLM filter. (c) Images adjusted by AHE. (d) Images labeled with detected pores for visualization. Images are displayed with adjusted contrasts.

4. XCT measurement

XCT measurements were carried out using a North Star[1] Imaging CXMM50 system [30] composed of a 225 kV source and a flat panel detector using acquisition parameters shown in Table 1. The parts are separated by slicing the base plate into rectangular blocks to keep the parts attached to pieces of the base plate (Fig. 3b) during XCT scan. This provides a reference plane for the XCT alignment. A custom-made holder was used to consistently hold the parts. XCT reconstruction was performed with efx-CT [31], which uses a Feldkamp-Davis-Kress algorithm [32].

Pores were detected in XCT images using an approach similar to Ref. [6]. Fig. 5 shows the major steps starting with the original XCT images in Fig. 5a. The XCT images are first filtered with a non-local mean (NLM) filter to reduce noise without significantly reducing image sharpness [33]. It smooths a target pixel by first taking a mean of all pixels in the image, and then weighted by how similar these pixels are to the target pixel. This results in greater clarity and less loss of detail in the image compared with the traditional local mean algorithms, which take only the mean value of a group of pixels surrounding the target pixel. The NLM filtered images are shown in Fig. 5b. The image is then adjusted with adaptive histogram equalization (AHE) to improve contrast [34]. AHE improves the local contrast by computing histograms of small regions in the image and uses them to redistribute the grayscale intensity values of the image. The AHE-adjusted images are shown in Fig. 5c. The AHE is processed slice by slice, and all the processed slices are then put into a 3D array to create an X-ray CT volume (XCTV). XCTV is then thresholded to determine the possible pores. A normal distribution curve is fitted into the XCTV data, and six standard deviations below the mean is determined as the threshold level. The volume and height of the determined pores are computed, any pores with a voxel count fewer than eight voxels are removed. Pores that are too small below this level could be noise in the images. Once the pores are identified, they are labeled by overlaying the pores on top of the image. Fig. 5d shows the labeled images.

Table 1
XCT acquisition parameters.

Parameter	Value
Voltage (kV)	220
Current (μA)	100
Target material	Tungsten
Filter (material; thickness (mm))	Cu; 3.05
Source-to-detector distance (mm)	432.0
Source-to-object distance (mm)	64.0
Magnification	6.8
Flat panel detector pixel size (μm)	127
Effective voxel pitch (μm)	18.8
Number of projections	1500
Frames per projection	1
frame rate (frames/s)	3
Beam hardening correction	No

In order to correlate the XCT results to the build process, the XCTV is first aligned to the build plate orientation and height. This is carried with the following steps:

(1) The XCTV is tilted to align with the AM build plane. Since the base plate is a part of the XCT images, the process is carried out by rotating the XCTV around the X- and Y-axes until the surface of the build plate stays within a single slice in Z direction.
(2) The XCTV is rotated around the Z-axis to align with the part orientation. The four distinctive shapes of the part corners assist with aligning the XCTV in the XY-plane. A line is drawn along the XCTV edge which is supposed to be parallel to the x-axis. The angle between this line and x-axis is determined, and the XCTV is rotated around Z-axis by this angle.
(3) The XCTV slice that corresponds to the first AM build layer is identified. For an LPBF process, the first powder layer is usually thicker to accommodate possible base plate surface waviness. On the AMMT, a laser probe is attached to the recoating arm to level the height of the base plate (10 cm × 10 cm build area) to within ±10 μm. Nevertheless, the thickness of the first layer is set to 50 μm, which is 30 μm thicker than following layers (20 μm each). Since the XCT slice thickness is its voxel pitch (18.8 μm, see

[1] Certain commercial equipment, instruments, or materials are identified in this paper in order to specify the experimental procedure adequately. Such identification is not intended to imply recommendation or endorsement by NIST, nor is it intended to imply that the materials or equipment identified are necessarily the best available for the purpose.

Table 1), the third XCT slice above the base plate slice is mapped to the first LPBF build layer.

(4) XCT slices are mapped to the LPBF build layers. In this study, the XCT slice thickness is 18.8 μm, the LPBF build layer thickness is 20 μm, and the height of the sample is 5 mm. Therefore, the top XCT slice is located at 5 mm/18.8 μm ≈ 266 slices above the first. These 266 XCT slices are interpolated and resampled into 250 slices, then each of these interpolated XCT slices corresponds to an LPBF build layer, with the same thickness of 20 μm. These interpolated/resampled XCT slices are referred to as XCT layers, to distinguish them from the XCT slices of the original sampling rate (18.8 μm). The mapping assumed a constant LPBF build layer thickness, this is only true for steady state. For the first few layers, the layer thickness will vary more due to the powder shrinkage [35].

The top surface of AM-built parts is not flat, and Fig. 6 shows the top 10 XCT layers (241–250) for the part built by the constant power scan strategy, the surface features extend to approximately 3–4 layers. The part built by constant power density scan strategy shows similar results. One interesting observation is that these top 10 layers (Fig. 6) have much fewer pores than the next 10 layers (Fig. 7). Most of the pores appear to extend through multiple LPBF layers, and two of them are marked as #1 and #2 in Fig. 7 traced by arrows through five consecutive layers (≈100 μm). The pore distribution shows radial patterns. There is a 67° layer-to-layer rotation, these island boundaries shift/rotate (radially) and their effects seem to extend to multiple layers, which result in radial patterns both on the top surface as well as the distribution of pores. The island boundaries of the top five layers were drawn and mapped to different XCT layers. With an offset of 15 layers, a good agreement was found between the pore locations and island boundaries as shown in Fig. 7 where the island boundaries for layers 246 to 250 are marked on layers 231 to 235. A concentration of pores is found along these boundaries. There are fewer pores found on the same layers built by the constant power density, as shown in Fig. 8.

The porosity can be obtained by the ratio of the voxels classified as pores to the total voxel in the 3D volume created from XCT images (XCTV). The porosity for the part built with the constant power scan strategy is 0.302%, and it was 0.099% for the constant power density. The detected pores can be further analyzed for their properties such as volume, height, centroid, and surface area. Fig. 9 shows pore height and volume distributions. The pore volume is the number of voxels in the pore, and the pore height is the height of the bounding box of the pore in the Z-direction.

5. Digital twin of process monitoring

While XCT is a powerful tool to assess the part's quality, it is an expensive post-measurement process and the dimension it can measure for metal parts is usually limited to tens of millimeters depending on the system voltage. It would be helpful to develop an approach to predict the part quality during the build process. We propose d*igital twins of process monitoring* (DTPM) here, that are created from MP images and positions (at which they were taken). In this section, we use DTPM to investigate the formation of LOF defects and keyhole defects for both scan strategies.

5.1. High-speed meltpool imaging for 3D build

The build process was monitored in-situ by the MP monitoring camera (Fig. 2) at 10 kHz. The 10 kHz frame rate is equivalent to an inter-frame interval of 80 μm at 800 mm/s laser scan speed, which is comparable to the 85 μm laser spot size. We will explain why this is important later. A dual camera-link transmission is used with the frame grabber implemented with a field-programmable gate array (FPGA). The images acquired are streamed directly to the computer hard disk through FPGA DMA (direct memory access) channel. This allows virtually an unlimited number of images to be taken. A total of 4 712 040 8-bit grayscale MP images was collected for each part.

Figs. 10 and 11 show example MP images. An MP area (MPA) can be calculated by thresholding the MP images at a grayscale intensity corresponding to a measured melt pool solidification boundary. How to determine this threshold level will be discussed later. The positions where the MP images were taken are marked on the speed-power-MPA plots on the left of the images. The plots consist of a few scan lines. For the constant power build (Fig. 10), the laser slows down when it approaches the boundary until it stops completely at the boundary. Then, the scan moves to reach the starting position of the next line. Power is kept at its full scale until the scan completely stops and stays off until the next line starts. The MP areas in images 2 and 4 are larger than the rest. The laser will take approximately 50 μs to reach its full scale (per the previous calibration), which explains why the MP area in image 3 is not larger than in image 4, even though the scan speed is slower in image 3. For the constant power density build (Fig. 11), laser power is reduced when speed is slow, and the MP is more uniform.

Fig. 12 shows the distribution of the MP size for both parts. The constant power scan strategy creates more oversized MP (MPA >0.03 mm^2). Therefore, the constant power density scan strategy successfully kept the MP more constant by suppressing the oversized MP. Table 2. Summarize the MP statics and also compared the XCT porosity and laser input power consumption for the two builds. Overall, the constant power density scan strategy requires 15% less energy to build the same part with 67% less porosity. It also results in a 20% smaller average MP area, and 32% less MP area variation.

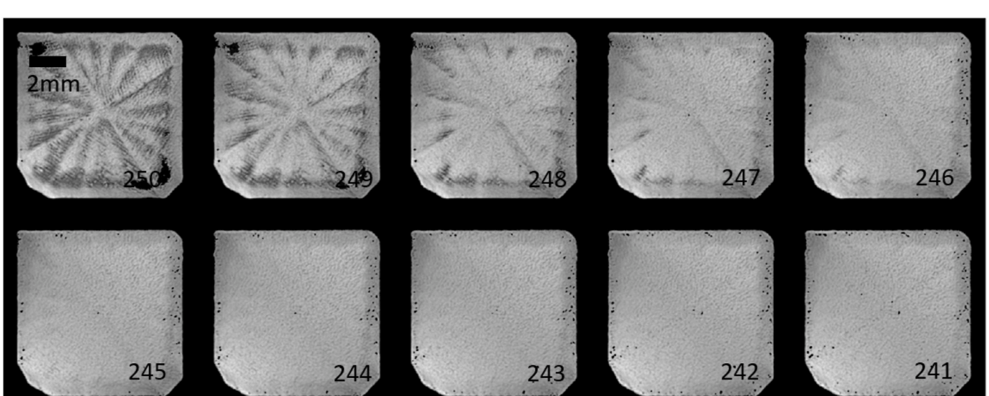

Fig. 6. XCT images of the part built with a constant power scan strategy for LPBF layers from 241 to 250.

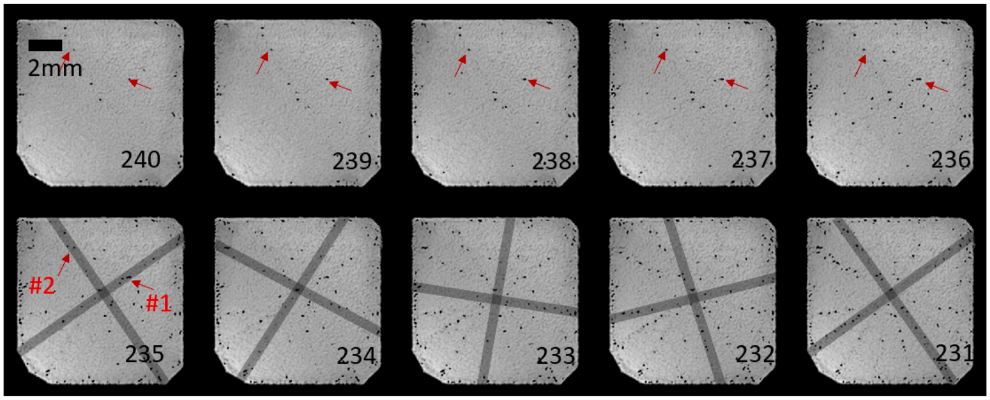

Fig. 7. XCT images for the part built with a constant power scan strategy, for layers 231 to 240. The thick gray lines on layers 231 to 235 are the island boundaries for layers 246 to 250, respectively. The arrows (#1 and #2) traced two pores (#1 and #2) across multiple layers.

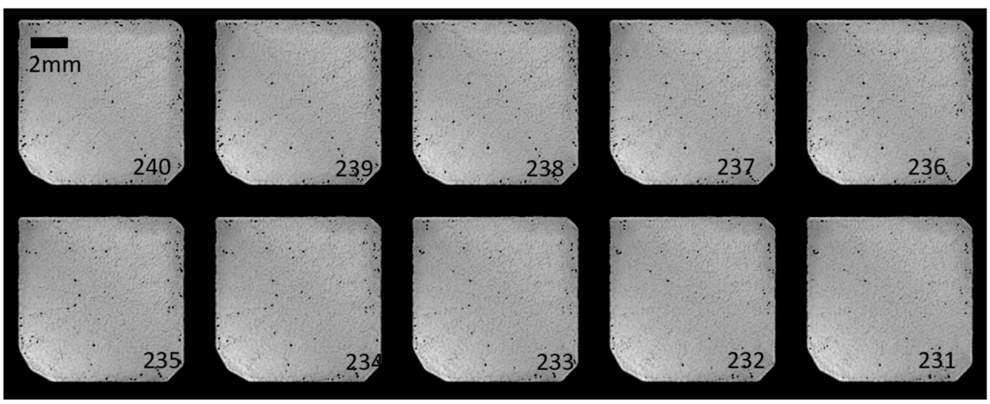

Fig. 8. XCT images of the part built with a constant power density scan strategy for layers 231 to 240.

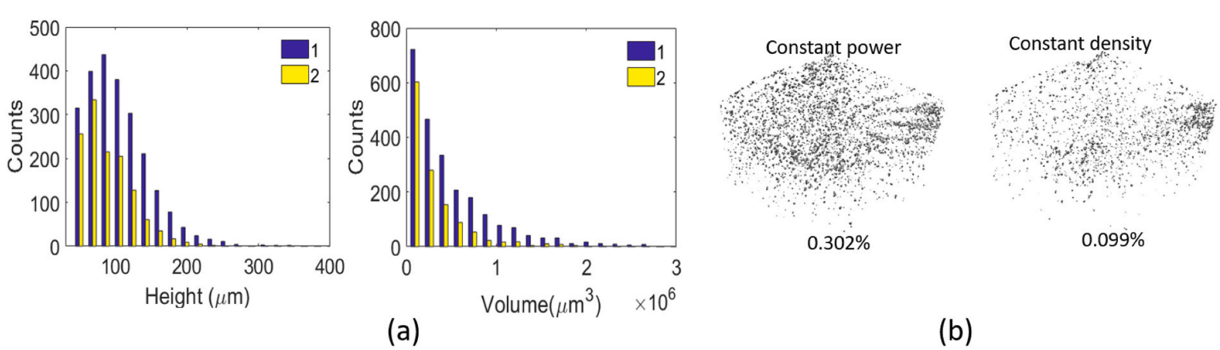

Fig. 9. Pores detected by XCT for parts built with (1) constant power and (2) constant power density scan strategies. (a) Pore height and volume. (b) Pore distribution.

5.2. Virtual MP intensity volume

If all the MP images taken for the layer are superimposed together, a virtual MP intensity (MPI) layer can be created. This is shown in Fig. 13. Fig. 13a shows four consecutive MP images taken from the constant power density build. The MP images were captured at 10 kHz. At speed of 800 mm/s, the inter-frame interval is 80 μm. This interval can be further reduced by interpolating the image along the scan path (Appendix A). Fig. 13b shows the MPI layer construction process, where the MP images were superimposed together at the positions they were taken. For the overlapped pixels, the maximum value is taken. This represents the maximum temperature each pixel ever experienced. More details on the MP image superimpose technique can be found in appendix A. Fig. 13c shows a completed MPI layer with MP images interpolated to an 8 μm interframe interval. The image is shown with enhanced contrast, but the track boundaries are still hardly visible. The islands are labeled per the scan sequence, the scan vector directions are marked by arrows. The track boundaries are more distinguishable in islands 1 and 2, likely because the part is cooler, and the MP width is smaller. The track boundaries are hardly visible for islands 3 and 4. The MPI layers are stacked together to create virtual MP intensity volume (MPIV), as shown in Fig. 13d. MPIV is stored as a 3D array, the array elements can be thought of as grayscale voxels with horizontal resolution same as the MP image pixel, and vertical resolution equals the build layer thickness.

The MPIV records the highest temperature (in the grayscale intensity

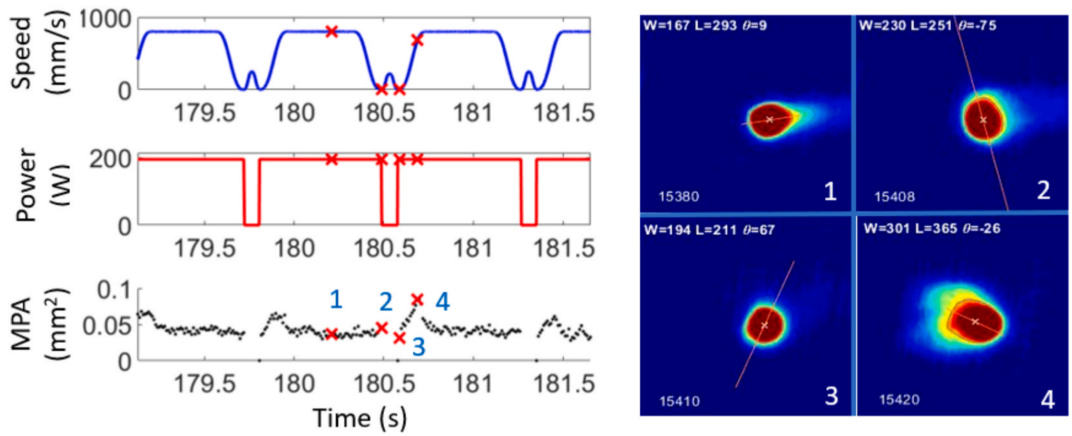

Fig. 10. Constant power scan. MPA plotted together with laser speed and power are shown on the left, MP images (pseudo color) at locations marked by 'x' are shown on the right. (For interpretation of the references to color in this figure legend, the reader is referred to the Web version of this article.)

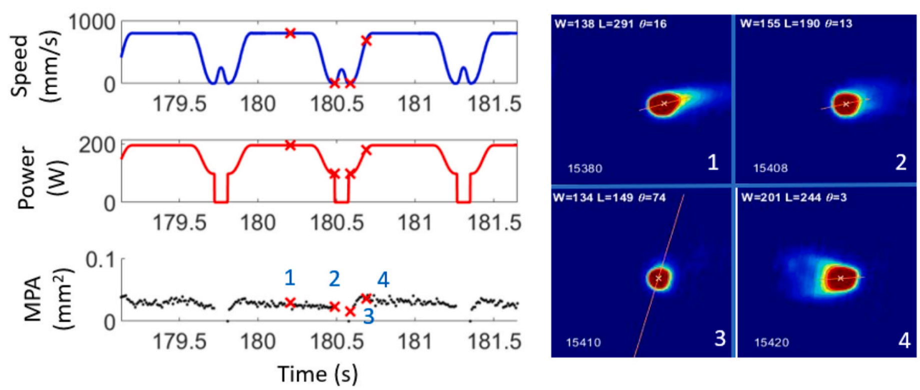

Fig. 11. Constant power density scan. MPA plotted together with laser speed and power are shown on the left, MP images (pseudo color) at locations marked by 'x' are shown on the right. (For interpretation of the references to color in this figure legend, the reader is referred to the Web version of this article.)

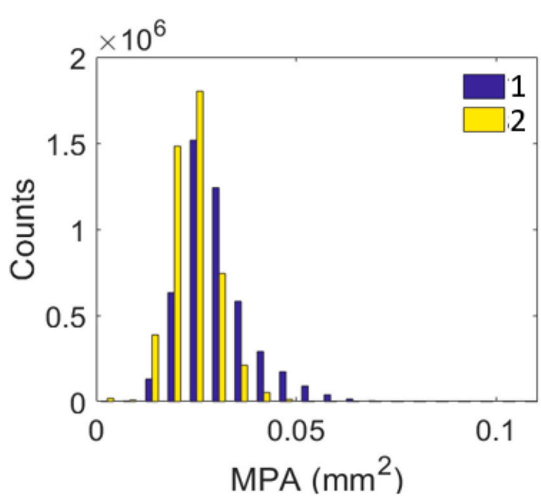

Fig. 12. MP area distribution for parts built by (1) constant power and (2) constant power density.

scale) that each voxel ever experienced. A threshold corresponding to the melting temperature can be applied to MPIV to determine the locations where the temperature had not reached the melting point. That is, to predict the LOF defects. This threshold was determined to be the grayscale 100 from the previous calibration. Details can be found in Appendix A. Once the MPIV is thresholded, the same algorithm used for

Table 2
Comparison of the two scan strategies.

Scan strategy	Total laser energy (kJ)	XCT pore density	MP area mean (mm^2)	MP area std (mm^2)
Constant power	85.99	0.302%	0.0297	0.0087
Constant power density	73.26	0.099%	0.0239	0.0059
Improvement	15%	67%	20%	32%

the porosity detection of the threshold XCTV can be applied to the MPIV. At the threshold of grayscale 100, 0% porosity is detected for both the constant power and constant power density parts. Indeed, AMMT is a well-calibrated machine, with well-planned scan paths and jerk-limited motion control [26], all areas should be fully covered. The LOF defects could also be triggered stochastically by plume or ejecta [36], but they can as well be captured by the MP images. An example is given in Fig. 14, where single tracks were scanned with gas flow turned off. The plume accumulated and interfered with both the incoming heating laser beam and emitted light from the MP. The effect The MP images captured these abnormalities, as shown by the virtual MP tracks in Fig. 14c. The complete study is published in Ref. [23].

For the purpose of comparison, the MPIVs are thresholded at grayscale of 250. Fig. 15 shows the result from the 3D build. The 'porosity' for constant power is 0.006%, whereas for constant power density, it is 0.120%. The trend is opposite of the porosity measured by XCT. The average MP area from the constant power build tends to be larger than that of the constant power density build (Fig. 12), hence it covers the

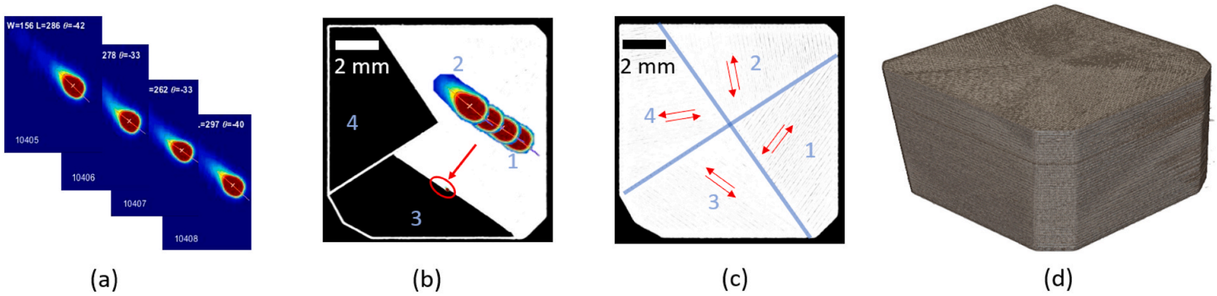

Fig. 13. Construction of MPIV. (a) MP image sequence. (b) MPI layer construction process. (c) MPI layer constructed. (d) MPIV constructed.

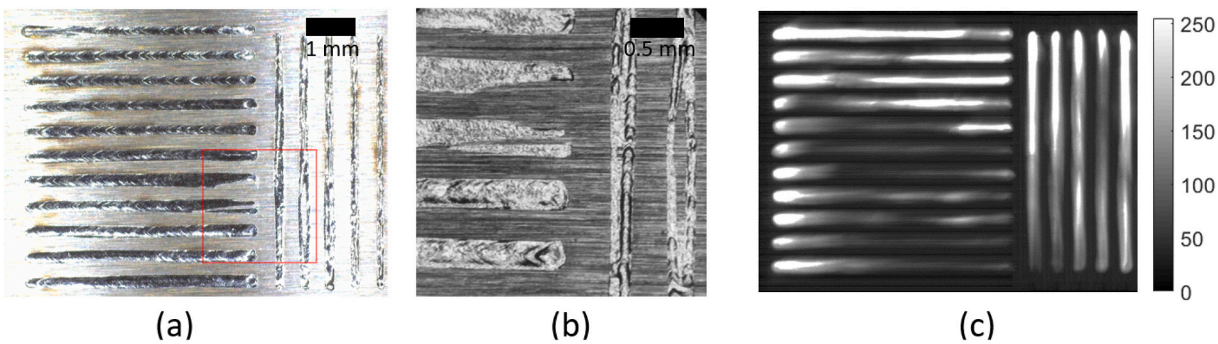

Fig. 14. Single-track experiments show LOF defects captured by the in-situ MP imaging. (a) Microscopic image of the single tracks. (b) Enlarged view for the region in the red rectangle. (c) The virtual MP tracks created from MP images. The color bar on the right shows the grayscale intensity of the MP images.

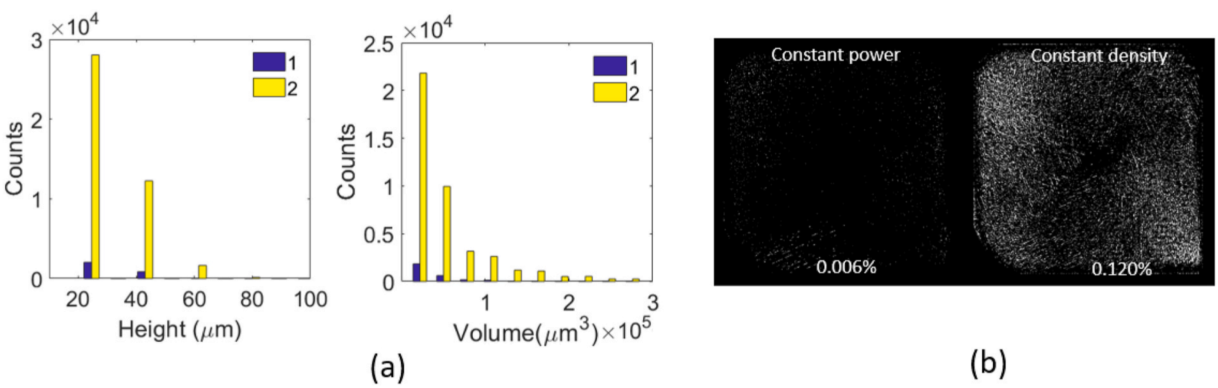

Fig. 15. Lack of fusion pores detected by thresholding MPIV created with (1) constant power and (2) constant power density. (a) Pore height and volume distributions. (b) Pores pattern by superimposing all layers. The pores for constant power are virtually invisible.

build area better. The pore height distribution shows that most pores are less than three layers high. The current MPIV model has not considered the re-melting effect from the layer above, which could have further reduced un-melted regions. This indicates that the pores, especially multi-layer pores detected by XCT (Fig. 9), are unlikely to be LOF defects.

Under normal build conditions, the MP depth is usually larger than the powder layer thickness. A layer can be re-melted multiple times by the scans above. This re-melting effect can be taken into consideration by estimating the MP depth from the scan parameters and MP areas from the analytic model developed in Refs. [37,38]. A machine learning model can also be developed to predict the MP 3D morphology from the MP images. Nevertheless, the LOF predictions made by MPIV without the re-melting effect may have many false-positive cases (the predicted defect is not actually a defect), but should not have any true-negative cases (the actual defect is not predicted).

5.3. Meltpool area volume

A meltpool area (MPA) map can be created by assigning the MPA values to the locations (the point) where each MP image was taken. Fig. 16 shows the MPA maps for the last five layers of both parts. The MPA maps for the constant power part in Fig. 16a show a concentration of large MP near the island boundaries. These are the beginnings and ends of the scan lines, where the energy density is high since the laser scan speed is slow. The MPA maps for the constant power part in Fig. 16b show much less variation, evidence that the constant power density strategy has efficiently suppressed the oversized MPs when the scan speed is slow.

An alternative way to create an MPA map is by assigning the MPA values to the *areas* where each MP image occupies. This approach is similar to creating the virtual MPI layers in Fig. 13, but the grayscale intensity value of the MP image is replaced by its MP area (normalized to 255). Fig. 17 shows the top five layers of the MPA maps created for both

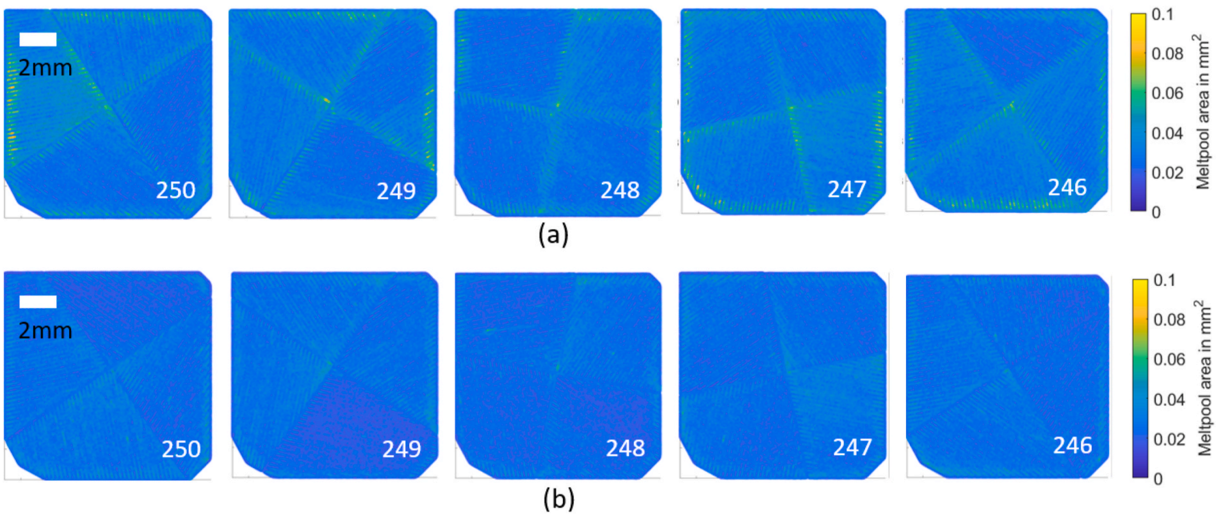

Fig. 16. MPA maps created by assigning the MPA values to the locations (points) where each MP image was taken. (a) Constant power. (b) Constant power density.

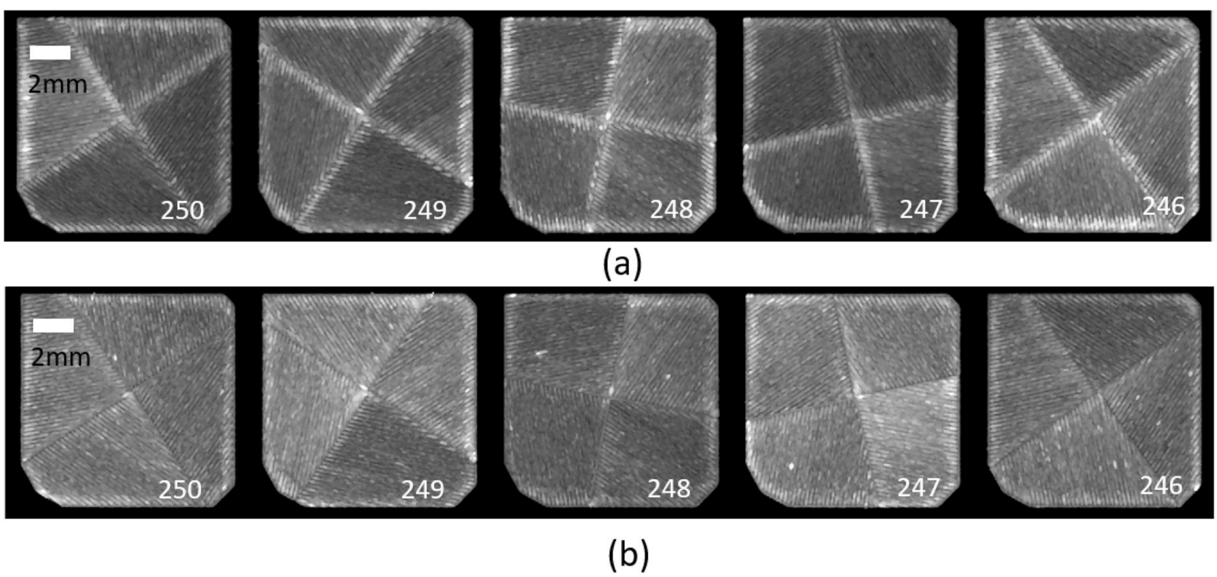

Fig. 17. MPA maps created by assigning the MPA values to the areas where each MP image occupies. (a) Constant power. (b) Constant power density.

parts. Again, constant power mode creates a lot of oversize MP along the island boundaries. An MPA volume (MPAV) is created by stacking the MPA maps together. The voxel value of MPAV represents the maximum MPA value it has ever experienced. If an assumption can be made that an oversized MP indicates a potential keyhole pore underneath, the MPAV can then be used to predict keyhole pores, like MPIV is used to predict the LOF pores.

Comparing the locations/distributions of pores on the XCT layers and the oversized MP on the MPA maps, the following observations/comments can be made:

1. There are very few pores in the top 10 layers (Fig. 6). Pores increase gradually when moving down the next 10 layers (Fig. 7). The pores in the lower 10 layers could be created by the scans from the upper 10 layers, this agrees with the in-situ X-ray observation in Ref. [8] where keyhole pores can be created 200 μm (10 layers) below the current scan layer; and is consistent with simulation results for keyhole pore formation in Ref. [16].
2. There is a concentration of large MP along the island boundaries for all layers Fig. 17a). A similar pattern is observed on the XCT layers (Fig. 7) but 10 to 15 layers lower. A possible explanation is that the oversized MP caused keyhole pores formation extending 10 to 15 layers below in addition to a potential residual error in the spatial registration.
3. The pore height distribution in Fig. 9 shows a peak around four layers for the part built by constant power. This distribution agrees with the observation in Fig. 7, where most pores extend multiple layers.
4. The pore height distribution in Fig. 9 shows some pores in the constant power part extend more than 10 layers. It is not clear how the pores of this height are formed, but [9] shows keyholes with a depth of 400 μm are not uncommon.

The above shows MPA maps could be potentially used to predict the keyhole pores. Since not necessarily all oversized MP will end up keyholes, and not all keyholes will end up pores, this prediction could have a lot of false-positive cases. Nevertheless, MPA maps or MPAV should be a good indication of the overall porosity level. It is shown a more uniform MPA map (Fig. 17b) indicates fewer keyhole pores (Fig. 8). More advanced tools, such as deep learning algorithms, can be applied to further improve such predictions.

6. Conclusion

For a laser powder bed fusion additively manufacturing process, the laser power density depends on both laser power and speed. Previous studies show keyhole pores are likely to form if the laser power density is too high. If the laser power is set constant, this could happen at begin/end of the scan while the steady speed has not reached. A simple solution to this is a constant laser power density scan strategy, to vary the laser power based on scan speed. However, its implementation requires a continuous variation of laser power, and complete synchronization of laser power to the laser scan speed and position. Probably for this reason, its application on 3D builds has not been reported before. In this study, we implemented a constant laser power scan strategy on a custom-built testbed and used it to build 3D nickel alloy 625 cubic parts. Compared to the commonly used constant laser power approach, the part requires 15% less energy to build and has 67% less porosity.

Two digital twins of process monitoring, MPIV and MPAV, were constructed to investigate the scan strategy effect on porosity. The MPIV and MPAV have their unique advantages and address different pore formation phenomena. Different analyses will be necessary to extract signatures from different defect formation phenomena such as surface LOF and keyhole porosity. A combination of analysis methods, or additional measurement techniques, will ultimately be necessary to identify a majority of occurrences of in-process defect formation. The mechanisms for defect formation are not easily distinguishable in XCT, which gives a 'total' count of pores. Therefore, comparison of only one in-situ measurement and analysis technique (e.g., MPIV or MPAV) to XCT porosity, will underpredict the amount of porosity measured via XCT. Overall, the DTPM provides a foundation for the future development of machine learning models, and the goal is to use digital twins for in-process feedback control and quality prediction.

Credit author statement

H. Yeung: Conceptualization, Methodology, Software, Writing – original draft, **F.H. Kim**:Data curation, Investigation, Writing – review & editing, **M. A. Donmez**: Writing – review & editing, Project administration, J. **Neira**: Investigation

Declaration of competing interest

The authors declare that they have no known competing financial interests or personal relationships that could have appeared to influence the work reported in this paper.

Data availability

No data was used for the research described in the article.

Appendix A. Meltpool image superimpose technique

Figure A1 explains the meltpool (MP) image superimpose technique. MP images from a single-track experiment were used to demonstrate the technique. Unlike 3D builds, the total number of images that need to be captured for a single track is small, so camera on-board memory can be utilized; hence the frame rate can be set extremely high. The single track was scanned on a bare metal plate, with a laser speed of 500 mm/s and laser power of 400 W. The track is 10 mm long, the scan process was imaged at 50 kHz, and so the inter-frame interval is 10 μm.

The MP image sequences in (a) to (c) are extracted from the single-track MP image sequence by taking out one frame at every 50, 25, and 10 frames. Therefore, the equivalent frame rates are 1 kHz, 2 kHz, and 5 kHz, and the equivalent inter-frame intervals are 500 μm, 250 μm, and 100 μm. For each sequence, upper rows (labeled as 1 in the figure) are created by superimposing the MP images at the positions they were taken, and according to the sequence they were taken. As the inter-frame interval reduces from (a) to (c), the tails of the front MP images overlap more with the heads of the back MP images. If the images are superimposed by taking the maximum grayscale values of the overlapped pixels instead, the virtual MP tracks in lower rows (labeled as 2 in Figure A1) are created. The grayscale intensity of the MP images is linearly related to the surface radiant emission, which is exponentially related to the surface temperature. The highest grayscale value for each pixel on the virtual track is monotonically related to the highest associated surface temperature it experienced. A smaller inter-frame interval will create a smoother virtual MP track, but it also means a higher image streaming rate is required for a 3D build. Figure A1d shows an alternative approach to create a smoother track. While the inter-frame interval is the same as Figure A1c at 100 μm, each interval is further divided into 10 subintervals and the same image is superimposed on these 10 interpolated positions. A much smoother track is produced in Figure A1d. Through this method, a continuous, interpolated virtual MP track may be formed in lieu of a high MPM camera frame rate.

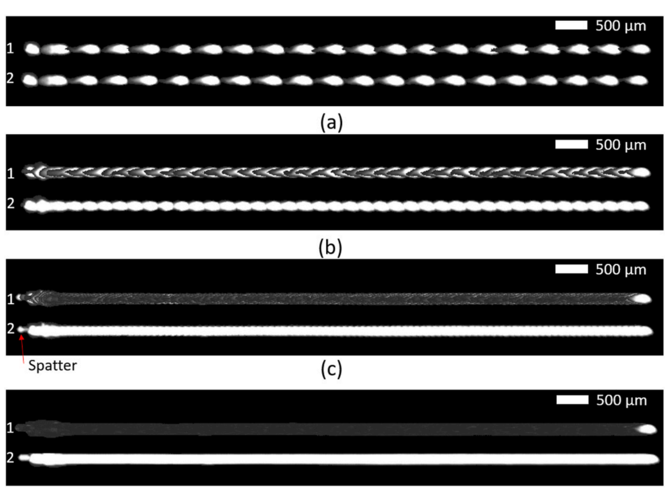

Fig. A1. Virtual MP tracks created with MP images (two different methods of superimposing MP images shown in the rows labeled as 1 and 2) sampled at the inter-frame interval of (a) 500 μm, (b) 250 μm, (c) 100 μm, and (d) 100 μm, but interpolated to 10 μm.

Fig. A2compares the microscopic images of the physical track with the virtual MP track created with full frames from the original sequence. Four sample MP images are also shown in Fig. A2c, the position for image 1 is marked on the physical track (Fig. A2a) by its chevron shape. Image 2 was triggered at the same time step as the laser power was commanded to turn off. Images 3 and 4 were triggered at 100 μs and 260 μs respectively after the laser power is turned off. The chevron patterns on the virtual MP track Fig. A2bare created by the boundaries of the MP tails, to demonstrate the level of details the MP images can capture. The chevron pattern is not part of the virtual MP track.

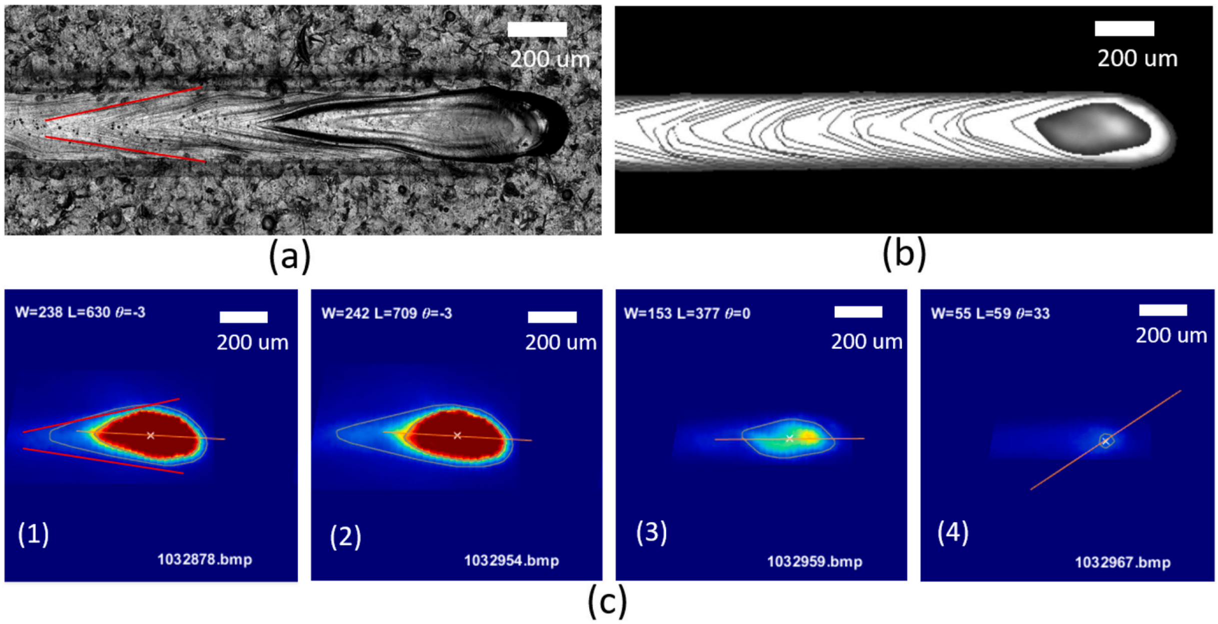

Fig. A2. Physical track and virtual MP track comparison. (a) The microscopic image of the physical track. (b) Virtual MP track created by MP images. (c) Sample MP images (pseudocolor). The chevron shape of image 1 is marked on the physical track. The chevron on the virtual MP track is created from the boundaries of the MP tails.

Once the virtual MP track is created, it can be thresholded to determine the track width. The track width can also be determined from the microscopic image of the physical track. This is shown in Fig. A3. The apparent difference between the physical and virtual tracks at the beginning of the track in Fig. A3is caused by a spatter. A spatter disconnected from the MP can be easily isolated and excluded from the virtual MP track construction, but this spatter is connected to the MP as shown in Fig. A1. Spatters are more frequently seen when scanned with powder. This is one limitation of this virtual MP track creation technique. Nevertheless, the virtual MP track in Fig. A1is a very close approximation of the physical track.

The width of the physical track is determined by the difference between the upper and lower hand-traced boundaries (Fig. A3a). This physical track width is then used to determine the threshold level for the virtual track. Virtual MP track widths measured with different threshold levels are compared with the physical track width (Fig. A3c). The threshold level that gives the minimum difference is determined as the grayscale intensity corresponding to the melting temperature. This grayscale value is used to threshold MP images to calculate the MP areas, such as in Figs. 13–12; and to determine the LOF defects in the virtual MP intensity volume built with this superimpose technique.

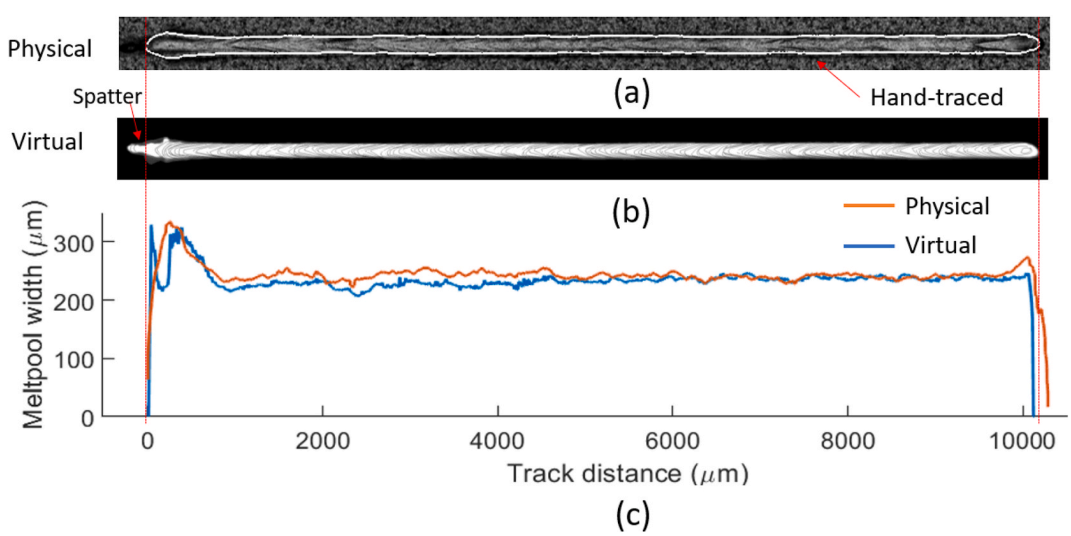

Fig. A3. MP width measurement. (a) Microscopic image of the physical track. The track boundaries are hand traced and marked by white lines. (b) Virtual MP track created by MP images. (c) Comparison of the track widths measured from (a) and (b).

The meltpool (MP) image superimpose technique introduced here is an extension of the author's previous work in Ref. [7], where MP images were stitched together to determine the subsurface LOF pores caused by the synchronization and following errors in the laser control. The technique is further improved here with the MP image interpolation method (Fig. A1) to create a virtual track with a smooth boundary, and hence prevent false LOF prediction.

References

[1] M. Mani, B. Lane, A. Donmez, S. Feng, S. Moylan, R. Fesperman, Measurement Science Needs for Real-Time Control of Additive Manufacturing Powder Bed Fusion Processes, National Institute of Standards and Technology), 2015.

[2] M. Grasso, B.M. Colosimo, Process defects and in situ monitoring methods in metal powder bed fusion: a review, Meas. Sci. Technol. 28 (2017), 044005.

[3] H. Shipley, D. McDonnell, M. Culleton, R. Coull, R. Lupoi, G. O'Donnell, D. Trimble, Optimisation of process parameters to address fundamental challenges during selective laser melting of Ti-6Al-4V: a review, Int. J. Mach. Tool Manufact. 128 (2018) 1–20.

[4] S. Sanchez, P. Smith, Z. Xu, G. Gaspard, C.J. Hyde, W.W. Wits, I.A. Ashcroft, H. Chen, A.T. Clare, Powder Bed Fusion of nickel-based superalloys: a review, Int. J. Mach. Tool Manufact. 165 (2021), 103729.

[5] X. Li, Q. Guo, L. Chen, W. Tan, Quantitative investigation of gas flow, powder-gas interaction, and powder behavior under different ambient pressure levels in laser powder bed fusion, Int. J. Mach. Tool Manufact. 170 (2021), 103797.

[6] F.H. Kim, S.P. Moylan, E.J. Garboczi, J.A. Slotwinski, Investigation of pore structure in cobalt chrome additively manufactured parts using X-ray computed tomography and three-dimensional image analysis, Addit. Manuf. 17 (2017) 23–38.

[7] F.H. Kim, H. Yeung, E.J. Garboczi, Characterizing the effects of laser control in laser powder bed fusion on near-surface pore formation via combined analysis of in-situ melt pool monitoring and X-ray computed tomography, Addit. Manuf. 48 (2021), 102372.

[8] W.E. King, H.D. Barth, V.M. Castillo, G.F. Gallegos, J.W. Gibbs, D.E. Hahn, C. Kamath, A.M. Rubenchik, Observation of keyhole-mode laser melting in laser powder-bed fusion additive manufacturing, J. Mater. Process. Technol. 214 (2014) 2915–2925.

[9] H. Gong, K. Rafi, H. Gu, T. Starr, B. Stucker, Analysis of defect generation in Ti–6Al–4V parts made using powder bed fusion additive manufacturing processes, Addit. Manuf. 1 (4) (2014) 87–98.

[10] S.A. Khairallah, A.T. Anderson, A. Rubenchik, W.E. King, Laser powder-bed fusion additive manufacturing: physics of complex melt flow and formation mechanisms of pores, spatter, and denudation zones, Acta Mater. 108 (2016) 36–45.

[11] S. Shrestha, T. Starr, K. Chou, A study of keyhole porosity in selective laser melting: single-track scanning with micro-CT analysis, J. Manuf. Sci. Eng. 141 (2019), 071004.

[12] A.A. Martin, N.P. Calta, S.A. Khairallah, J. Wang, P.J. Depond, A.Y. Fong, V. Thampy, G.M. Guss, A.M. Kiss, K.H. Stone, C.J. Tassone, J. Nelson Weker, M. F. Toney, T. van Buuren, M.J. Matthews, Dynamics of pore formation during laser powder bed fusion additive manufacturing, Nat. Commun. 10 (2019), 1987.

[13] R. Cunningham, C. Zhao, N. Parab, C. Kantzos, J. Pauza, K. Fezzaa, T. Sun, A. D. Rollett, Keyhole threshold and morphology in laser melting revealed by ultrahigh-speed x-ray imaging, Science 363 (2019) 849–852.

[14] S.M.H. Hojjatzadeh, N.D. Parab, Q. Guo, M. Qu, L. Xiong, C. Zhao, L.I. Escano, K. Fezzaa, W. Everhart, T. Sun, L. Chen, Direct observation of pore formation mechanisms during LPBF additive manufacturing process and high energy density laser welding, Int. J. Mach. Tool Manufact. 153 (2020), 103555.

[15] Q. Guo, M. Qu, L.I. Escano, S.M.H. Hojjatzadeh, Z. Young, K. Fezzaa, L. Chen, Revealing melt flow instabilities in laser powder bed fusion additive manufacturing of aluminum alloy via in-situ high-speed X-ray imaging, Int. J. Mach. Tool Manufact. 175 (2022), 103861.

[16] L. Wang, Y. Zhang, H.Y. Chia, W. Yan, Mechanism of keyhole pore formation in metal additive manufacturing, Npj Comput. Mater 8 (2022) 22.

[17] C. Tan, F. Weng, S. Sui, Y. Chew, G. Bi, Progress and perspectives in laser additive manufacturing of key aeroengine materials, Int. J. Mach. Tool Manufact. 170 (2021), 103804.

[18] The Gemini Principles, Centre for Digital Built Britain, 2018. Retrieved 2020-01-01, www.cdbb.cam.ac.uk.

[19] T. DebRoy, W. Zhang, J. Turner, S.S. Babu, Building digital twins of 3D printing machines, Scripta Mater. 135 (2017) 119–124.

[20] G.L. Knapp, T. Mukherjee, J.S. Zuback, H.L. Wei, T.A. Palmer, A. De, T. DebRoy, Building blocks for a digital twin of additive manufacturing, Acta Mater. 135 (2017) 390–399.

[21] T. Mukherjee, T. DebRoy, A digital twin for rapid qualification of 3D printed metallic components, Appl. Mater. Today 14 (2019) 59–65.

[22] L.E. Criales, Y.M. Arısoy, B. Lane, S. Moylan, A. Donmez, T. Özel, Laser powder bed fusion of nickel alloy 625: experimental investigations of effects of process parameters on melt pool size and shape with spatter analysis, Int. J. Mach. Tool Manufact. 121 (2017) 22–36.

[23] D.C. Deisenroth, J. Neira, J. Weaver, H. Yeung, Effects of Shield Gas Flow on Meltpool Variability and Signature in Scanned Laser Melting ASME 2020 15th International Manufacturing Science and Engineering Conference, American Society of Mechanical Engineers), 2020. V001T01A017.

[26] H. Yeung, B.M. Lane, M.A. Donmez, J.C. Fox, J. Neira, Implementation of advanced laser control strategies for powder bed fusion systems, 46th SME North Am. Manuf. Res. Conf. NAMRC 46 Tex. USA 26 (2018) 871–879.

[27] Yeung H Hutchinson, Keely J and Lin, Dong B Design and implementation of laser powder bed fusion additive manufacturing testbed control software Solid Free. Fabr. 2021 Proc. 32th Annu. Int. Solid Free. Fabr. Symp.

[28] Lane, et al., Design, developments, and results from the NIST additive manufacturing Metrology testbed (AMMT), Solid Free. Fabr (2016). Proc. 26th Annu. Int. Solid Free. Fabr. Symp.

[29] H. Yeung, J. Neira, B. Lane, J. Fox, F. Lopez, Laser path planning and power control strategies for powder bed fusion systems, Solid Free. Fabr (2016). Proc. 27th Annu. Int. Solid Free. Fabr. Symp.

[30] North Star Imaging NSI CXMM50. https://4nsi.com/innovations/metrology/.

[31] North Star Imaging efX-CT. https://4nsi.com/software/efx-ct.

[32] L.A. Feldkamp, L.C. Davis, J.W. Kress, Practical cone-beam algorithm, J. Opt. Soc. Am. A 1 (1984) 612.

[33] A. Buades, Coll B and Morel J-M 2005 A Non-local Algorithm for Image Denoising 2005 IEEE Computer Society Conference on Computer Vision and Pattern Recognition (CVPR'05), in: IEEE Computer Society Conference on Computer Vision and Pattern Recognition (CVPR'05), vol. 2, IEEE), San Diego, CA, USA, 2005, pp. 60–65.

[34] S.M. Pizer, E.P. Amburn, J.D. Austin, R. Cromartie, A. Geselowitz, T. Greer, B. ter Haar Romeny, J.B. Zimmerman, K. Zuiderveld, Adaptive histogram equalization and its variations, Comput. Vis. Graph Image Process 39 (1987) 355–368.

[35] H. Chen, T. Cheng, Z. Li, Q. Wei, W. Yan, Is high-speed powder spreading really unfavourable for the part quality of laser powder bed fusion additive manufacturing? Acta Mater. 231 (2022), 117901.

[36] A.R. Nassar, M.A. Gundermann, E.W. Reutzel, P. Guerrier, M.H. Krane, M. J. Weldon, Formation processes for large ejecta and interactions with melt pool formation in powder bed fusion additive manufacturing, Sci. Rep. 9 (2019) 5038.

[37] R. Fabbro, Scaling laws for the laser welding process in keyhole mode, J. Mater. Process. Technol. 264 (2019) 346–351.

[38] R. Fabbro, M. Dal, P. Peyre, F. Coste, M. Schneider, V. Gunenthiram, Analysis and possible estimation of keyhole depths evolution, using laser operating parameters and material properties, J. Laser Appl. 30 (2018), 032410.